ADVANCED FUNCTIONAL MATERIALS
www.afm-journal.de

Investigating the Role of Emissive Layer Architecture on the Exciton Recombination Zone in Organic Light-Emitting Devices

*Nicholas C. Erickson and Russell J. Holmes**

An experimental approach to determine the spatial extent and location of the exciton recombination zone in an organic light-emitting device (OLED) is demonstrated. This technique is applicable to a wide variety of OLED structures and is used to examine OLEDs which have a double- (D-EML), mixed- (M-EML), or graded-emissive layer (G-EML) architecture. The location of exciton recombination in an OLED is an important design parameter, as the local optical field sensed by the exciton greatly determines the efficiency and angular distribution of far-field light extraction. The spatial extent of exciton recombination is an important parameter that can strongly impact exciton quenching and OLED efficiency, particularly under high excitation. A direct measurement of the exciton density profile is achieved through the inclusion of a thin, exciton sensitizing strip in the OLED emissive layer which locally quenches guest excitons and whose position in the emissive layer can be translated across the device to probe exciton formation. In the case of the G-EML device architecture, an electronic model is developed to predict the location and extent of the exciton density profile by considering the drift, diffusion, and recombination of charge carriers within the device.

1. Introduction

Organic light-emitting devices (OLEDs) are attractive for use in display and lighting applications due to their demonstrated high efficiency, spectral tunability, and compatibility with high-throughput manufacturing techniques. In phosphorescent OLEDs, high external quantum efficiencies (η_{EQE}) have been realized using a variety of device architectures with varying degrees of complexity.[1–11] As understanding of the fundamental processes relevant for efficient device operation has improved, models of the optical and electronic characteristics of multilayer devices have become increasingly predictive.[12–14] One important feature of OLEDs which has proven difficult to probe experimentally is the spatial extent and location of the exciton recombination zone.[12] The spatial overlap between the exciton density and the local optical field greatly impacts the efficiency with which photons escape the device,[15–17] as well as the intrinsic radiative decay rate of the exciton.[12,18–20] The spatial extent of recombination has also been identified as an important parameter that governs the degree to which the η_{EQE} decreases under high excitation,[21–23] termed the efficiency "roll-off." The mechanisms responsible for the roll-off are separated into two general categories: a reduction in confinement in the emissive layer and bimolecular exciton quenching. The reduction in confinement at high drive current densities reduces the fraction of injected carriers which form excitons, and can be an obstacle to high efficiency operation.[22] However, such losses can often be mitigated through the use of charge carrier blocking layers that confine injected electrons and holes to the emissive layer. In terms of the bimolecular quenching of excitons, it is understood that in systems which employ long-lifetime phosphorescent emitters, triplet-triplet annihilation (TTA) and triplet-polaron quenching (TPQ) are the dominant mechanisms for roll-off at device-relevant electric fields, both of which are strongly dependent on the local density of excitons.[21–28]

As already noted, to achieve high peak η_{EQE} in an OLED effective exciton confinement is required in the emissive layer. This is often realized through the use of charge and exciton blocking layers with specific properties, including a shallow lowest unoccupied molecular orbital (LUMO) energy level to block electrons, a deep highest occupied molecular orbital (HOMO) energy level to block holes, or a large energy gap to confine excitons to the emissive layer. One challenge in multilayer devices which incorporate blocking layers is achieving balanced electron and hole injection into the emissive layer. Differences in the barrier heights and charge carrier mobilities for the electron and hole transport pathways inevitably lead to an emissive layer with an excess of one carrier type.[14] Additionally, the mobilities of electrons and holes often show different field dependencies,[29–31] further complicating charge balance across the useful range of drive voltages. As a result of this relative charge imbalance in the emissive layer, the recombination zone is likely pinned at the interface between the emissive layer and the minority carrier transport layer. In the absence

N. C. Erickson
Department of Electrical and Computer Engineering
University of Minnesota
Minneapolis, MN 55455, USA
R. J. Holmes
Department of Chemical Engineering and
Materials Science
University of Minnesota
Minneapolis, MN 55455, USA
E-mail: rholmes@umn.edu

DOI:10.1002/adfm.201300101

of substantial exciton diffusion or significant exciton quenching effects, the recombination zone is equivalent to the exciton generation profile, and is determined by the spatial overlap of the electron and hole charge densities in the emissive layer.

Device architectures which have shown improved charge balance and charge and exciton confinement often incorporate a double-emissive layer (D-EML) or mixed-emissive layer (M-EML).[3,5,6,32–34] The D-EML consists of two distinct layers, a hole-transport material (HTM) and an electron transport material (ETM), with an emissive guest uniformly doped throughout both layers. This design strongly confines the charge carriers to a region near the HTM:ETM interface.[5] The M-EML design consists of a uniformly mixed layer of HTM and ETM that is doped with a luminescent guest. This design has a large interfacial area between HTM and ETM to facilitate exciton formation and the charge carrier mobilities can be tuned by varying the ratio of HTM:ETM.[30,31,35] Both architectures are usually incorporated into multilayer structures to realize effective charge and exciton confinement.[3,36]

Conventional experimental determinations of the recombination zone in an OLED have focused on two techniques: translating the position of the guest emitter across the emissive layer while observing large changes in device performance, or monitoring the shape of the emission profile versus viewing angle and deducing the location of exciton generation based on weak microcavity effects.[31,37–42] While the former technique may give a qualitative determination of the recombination zone location, it gives little information about the recombination zone width and it neglects the often significant role played by the emissive guest in charge transport or charge injection into the emissive layer. This effect may be quite large, especially in devices which employ a single emissive layer where the host preferentially carries one type of charge, or use large doping concentrations where the guest may participate in charge transport.[40,43,44] The latter technique compares measured data to fits of optical models and is limited by assumptions present in the optical model.[41] A third technique which has recently been discussed employs a strip-doping method which relies on nearest-neighbor exciton quenching methods.[23,45] Use of this technique requires a high local concentration of a quenching molecule,[23,45] which may impact the electrical properties of the emissive layer.

In this work, the exciton recombination zone in various OLED emissive layer architectures is probed directly through the addition of a fluorescent sensitizer, capable of quenching excitons formed on the emissive guest, at different locations within the emissive layer. By comparing the overall emission intensity of sensitized devices to control structures containing no sensitizer, a 'map' of the local exciton density may be determined. Electrical measurements are performed to ensure that the inclusion of the sensitizer does not alter the electrical characteristics of the devices. This technique is applied to simplified OLEDs containing common emissive layer architectures, namely D-EML and M-EML-type structures, as well as an OLED based on a graded-emissive layer (G-EML), shown schematically in **Figures 1** a–c. The simplified structures facilitate comparisons of the recombination zones in the different devices and show the influence of emissive layer architecture on the recombination zone. The G-EML device offers an architecture which contains no sharp interfaces between HTM and ETM host layers or transport layers, and whose electronic character changes continuously with position within the device (see Figure 1d).[11,30,46] This device has been previously shown to exhibit a high degree of exciton and charge confinement, and is capable of realizing high efficiency in a single-layer device.[11] It is found that the G-EML and M-EML devices exhibit a large recombination zone while the D-EML exhibits a significantly narrowed recombination zone centered at the HTM:ETM interface. The larger recombination zones of the G-EML and M-EML may be responsible for an observed reduction in the efficiency roll-off compared to devices containing a D-EML.

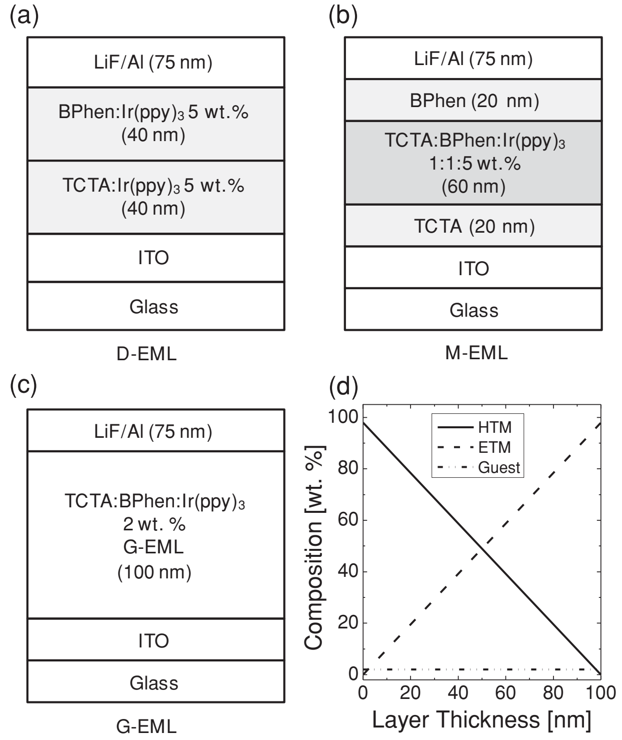

Figure 1. Layer structures for the a) double- (D-EML), b) mixed- (M-EML), and c) graded-emissive layer (G-EML) OLED architectures. The spatial composition profile (wt%) of the G-EML device is shown in (d).

This paper is organized as follows: a theoretical description of the exciton sensing technique and electronic model are presented in Section 2, results are analyzed and discussed in Section 3, and conclusions are presented in Section 4.

2. Theory

2.1. Exciton Sensitizing by Energy Transfer

Any technique designed to give a quantitative measurement of the exciton recombination zone requires: (i) a high sensitivity to the presence of guest excitons, (ii) a high degree of spatial resolution, and (iii) that it must not substantially alter the natural distribution of charge carriers or excitons within the device. One way to sense the recombination zone is by locally transferring excitons formed on the emissive guest to

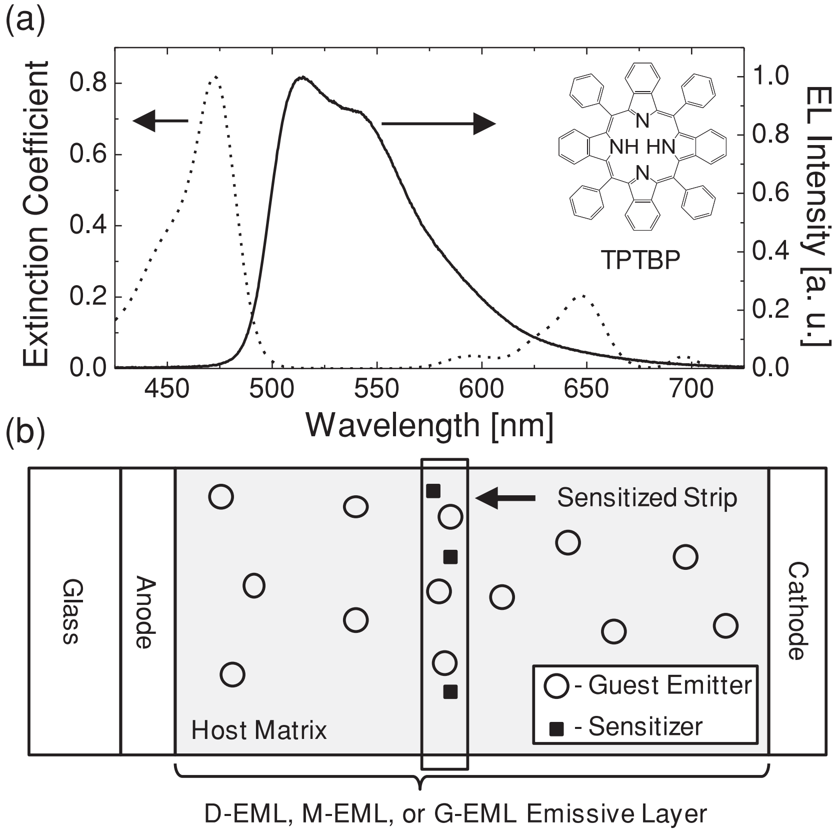

Figure 2. a) Extinction coefficient for the sensitizer, TPTBP (dashed line), and peak-normalized electroluminescence (EL) spectrum of the emissive guest, Ir(ppy)$_3$ (solid line). Inset: Molecular structure of TPTBP. b) Schematic representation of the sensitizing strip technique.

a second, "sensitizing" molecule.[23] Once the exciton is transferred from the guest to the sensitizer, it may be detected by monitoring emission from the sensitizer, or by selecting a sensitizing material which does not readily luminesce. In the later case the guest exciton is effectively quenched by the sensitizer, resulting in a measurable reduction in luminescence from the guest. Depending on the guest and sensitizing materials, quenching may occur via Dexter- or Förster-type energy transfer.[47,48] Quenching via Dexter energy transfer requires a physical exchange of electrons between the guest and sensitizer and is therefore a nearest-neighbor process. The rate of Dexter energy transfer falls off steeply with increasing separation between guest and sensitizer molecules.[48] While this mechanism may be a highly localized process, satisfying condition (ii), it requires a high density of sensitizer molecules in order to ensure that the sensitizer is adjacent to the dilute-doped guest, likely influencing the local electronic environment.[23] Förster energy transfer is a non-radiative dipole-dipole coupling between a donor (i.e., guest) and acceptor (i.e., sensitizer) molecule. This interaction may occur through occupied space, extending the range of energy transfer and quenching. The rate of Förster energy transfer between point dipoles is given by[49]:

$$k_F[d] = \frac{1}{\tau}\left(\frac{R_0}{d}\right)^6, \tag{1}$$

where τ is the exciton lifetime, d is the donor-acceptor molecular separation, and R_0 is the characteristic radius of Förster energy transfer, given by:[48,49]

$$R_0^6 = \frac{9\eta_{PL}\kappa^2}{128\pi^5 n^4}\int \lambda^4 F_D[\lambda]\sigma_A[\lambda]d\lambda, \tag{2}$$

where η_{PL} is the photoluminescence efficiency of the donor, κ is the dipole orientation factor, n is the index of refraction of the medium between the donor and acceptor, λ is the wavelength, F_D is the area-normalized donor emission spectrum, and σ_A is the absorption cross-section of the acceptor. Förster energy transfer between the guest and sensitizer, and thus the spatial resolution of exciton quenching, may be tuned by selecting a sensitizing material with an appropriate overlap of absorption with the guest emission. Quenching may then occur over a small distance (≈1–5 nm) and retain a high sensitivity to the presence of guest excitons, allowing a low sensitizer concentration to be used (<1 wt%). Such a low doping concentration is unlikely to affect charge transport and leads to only a slight reduction in spatial resolution.

In this work, a measurement of the recombination zone in a variety of common emissive layer architectures is realized by including a highly localized, lightly-doped strip of tetraphenyltetrabenzoporphyrin (TPTBP) into a device to quench excitons formed on the luminescent guest via Förster energy transfer. The composition of the sensitized strip is otherwise matched to the local concentrations of the host and guest materials for a particular structure. Here, TPTBP is selected based on the small overlap of its absorption cross section with the photoluminescence (PL) of the archetypical green phosphor, tris(2-phenylpyridine)iridium(III) (Ir(ppy)$_3$) (see **Figure 2**a). In a separate measurement, TPTBP showed extremely weak luminescence under electrical excitation, this ensures that excitons transferred from Ir(ppy)$_3$ predominantly decay non-radiatively. Subsequent measurements of the electroluminescence (EL) from sensitized devices containing both TPTBP and Ir(ppy)$_3$ showed no observable contribution from TPTBP. Using Equation 2 and the optical properties of TPTBP and Ir(ppy)$_3$, an R_0 = 3.9 nm is calculated. The Förster quenching distance, and thus the spatial resolution of the measurement, may be tuned by selecting a sensitizer with a small overlap of absorption with guest emission, ensuring a small R_0 and high degree of spatial resolution. The integrated EL intensity of each sensitized device is measured and compared to a control device which does not contain TPTBP, this quantity is termed the "EL ratio" ≡ β. This ratio is directly proportional to the ratio of quenched excitons and therefore the quantity 1-β is proportional to the ratio of unquenched excitons, i.e., the local exciton density. A map of the recombination zone is realized by fabricating a series of devices with the sensitizing strip translated throughout the emissive layer, and plotting the local exciton density versus strip position (Figure 2b). One factor that is not included but may become important in wide-recombination zone devices is the spatial dependence of the far-field extraction efficiency of excitons at different positions within the EML.

2.2. Electronic Model of the G-EML

Theoretical models for the spatial charge density in an organic semiconductor have previously been developed for multilayer OLEDs.[13,14,50] To describe the environment of a single-layer, G-EML device (Figure 1c), we adapt a model from Neumann et al. [51] which considers charge carrier drift, diffusion, and recombination to describe charge densities and the recombination zone. It is important to note that the charge densities, electric field, and mobility are all position dependent in a G-EML,[30] thus we have chosen to make this explicit by including [x] in all subsequent, spatially-dependent equations.

The one-dimensional equations are:

$$\frac{dF[x]}{dx} = \frac{e}{\varepsilon\varepsilon_0}(p[x] - n[x]), \tag{3}$$

$$\frac{dJ_n}{dx} = e\gamma n[x]p[x], \tag{4}$$

$$\frac{dJ_p}{dx} = -e\gamma n[x]p[x], \tag{5}$$

where Equation (3) is Poisson's equation. Here, *F*[x] is the electric field, *e* is the elementary charge, ε is the relative permittivity of the organic layer (taken here as $\varepsilon = 3$), ε_0 is the permittivity of vacuum, *p*[x] is the hole density, and *n*[x] is the electron density. The continuity equations for electrons and holes are given in Equations (4) and (5), respectively, and contain a Langevin-type recombination term. Langevin recombination has been extensively used to describe recombination in OLEDs.[47,52,53] In this formalism, γ is the recombination coefficient:

$$\gamma = \frac{e}{\varepsilon\varepsilon_0}(\mu_n[x] + \mu_p[x]). \tag{6}$$

The electron current density is given by:

$$J_n = e\,n[x]\mu_n[x]F[x] + kT\,\mu_n[x]\frac{dn[x]}{dx}, \tag{7}$$

and contains a field-dependent drift term as well as a diffusion term. Similarly, the hole current density is given by:

$$J_p = e\,p[x]\mu_p[x]F[x] - kT\,\mu_p[x]\frac{dp[x]}{dx}. \tag{8}$$

In these expressions we have assumed the validity of the Einstein relation relating the drift and diffusion of charge. To simplify the evaluation of the continuity equations, dimensionless quantities are used to describe the position, the electric field, and the charge densities:

$$X = \frac{1}{L}x, \tag{9}$$

$$E[X] = \frac{L}{V}F[X], \tag{10}$$

$$N[X] = n[X]\frac{L^2 e}{\varepsilon\varepsilon_0 V}, \tag{11}$$

$$P[X] = p[X]\frac{L^2 e}{\varepsilon\varepsilon_0 V}, \tag{12}$$

where *L* is the width of the G-EML layer and *V* is the applied voltage. Using the continuity equations and the electron and hole current densities defined in Equations (3)–(8), together with the dimensionless variables defined above, we derive four steady-state, coupled equations for the voltage, electric field and the carrier densities:

$$E[X] = -\frac{dV[X]}{dX}, \tag{13}$$

$$\frac{dE[X]}{dX} = P[X] - N[X], \tag{14}$$

$$\begin{aligned} 0 = &-N[X]^2 + N[X]E[X]\frac{d\mu_n[X]}{dX}\frac{1}{\mu_n[X]} + E[x]\frac{dN[X]}{dX} \\ &+ \frac{kT}{eV}\frac{d\mu_n[X]}{dX}\frac{1}{\mu_n[X]}\frac{dN[X]}{dX} \\ &+ \frac{kT}{eV}\frac{d^2N[X]}{dX^2} \\ &- N[X]P[X]\frac{\mu_n[X]}{\mu_p[X]}, \end{aligned} \tag{15}$$

$$\begin{aligned} 0 = &\ P[X]^2 + P[X]E[X]\frac{d\mu_p[X]}{dX}\frac{1}{\mu_p[X]} + E[x]\frac{dP[X]}{dX} \\ &+ \frac{kT}{eV}\frac{d\mu_p[X]}{dX}\frac{1}{\mu_p[X]}\frac{dP[X]}{dX} \\ &- \frac{kT}{eV}\frac{d^2P[X]}{dX^2}[x] \\ &+ N[X]P[X]\frac{\mu_n[X]}{\mu_p[X]}. \end{aligned} \tag{16}$$

While it is possible to write Poisson's equation in terms of *V* directly, it is instructive to solve for the shape of the field (as determined by *N*[X] and *P*[X]) while using *V* to set the boundary conditions. This matches well with actual device operation, where a potential is applied to the electrodes and the field may vary depending on the local electron and hole charge densities. The boundary conditions imposed are:

$$N[0] = P[1] = 0, \tag{17}$$

$$N[1] = P[0] = 1, \tag{18}$$

$$V[1] = 0, \tag{19}$$

$$V[0] = 1. \tag{20}$$

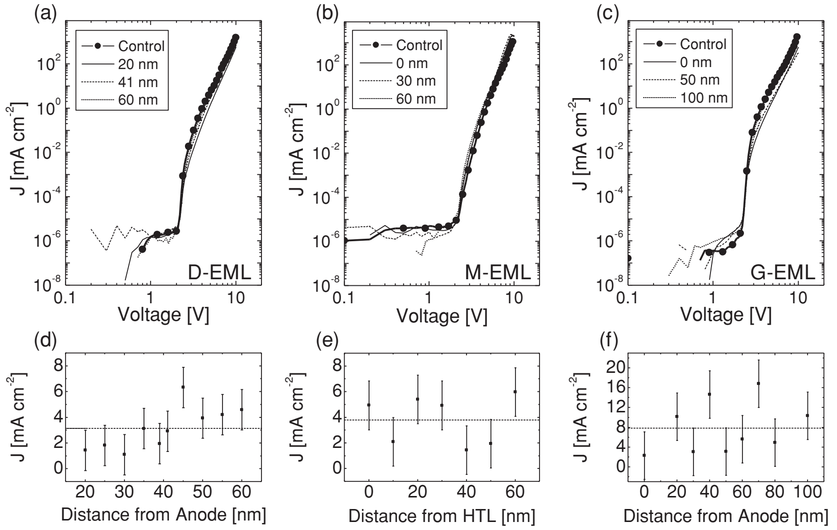

Figure 3. Current density–voltage characteristics (J–V) for a) D-EML, b) M-EML, and c) G-EML devices with a sensitizing strip located at different positions within the emissive layer (as measured from anode, in the case of the D-EML and G-EML, or from the TCTA/M-EML interface, for M-EML devices). Data for devices with intermediate strip positions are omitted for clarity. A control device which does not contain the sensitizing strip is shown (closed symbols) for each of the device architectures of interest. The current density at an applied voltage of 5 V for each device is shown in d) for D-EML devices, e) for M-EML devices, and f) for G-EML devices; the horizontal line represents the average current density of the devices and error bars are calculated from the current density variation of control devices fabricated in different runs.

The boundary conditions in Equation (17) constrain the system such that there is no electron leakage to the anode, no hole leakage to the cathode, and all current comes from the recombination of carriers. This scenario is valid given the high efficiencies previously obtained for single-layer G-EML OLEDs.[30] Together with the boundary conditions of Equation (18), an equal number of holes and electrons are present in the device. This last constraint ensures that the model reflects the steady-state behavior of the device and can be confirmed by comparing the integrated charge densities. The boundary conditions of Equations (19) and (20) reflect a system where one side is grounded and a potential is applied at the opposite side. The magnitude of the applied voltage is varied in the coupled equations. Finally, the product of the electron (*N*[X]) and hole (*P*[X]) charge densities (the 'NP product') is equivalent to the exciton density profile, and thus reflects the extent of the exciton recombination zone with exciton diffusion assumed to be negligible. This last assumption is valid for cases where the exciton is well-confined to the guest and the guest concentration is low, both of which are typical conditions in an OLED.

3. Results and Discussion

3.1. Recombination Zone Determination

The current density–voltage (J–V) characteristics for selected sensitized devices are shown in **Figures 3**a–c for D-EML, M-EML, and G-EML devices, respectively, as a function of strip position, along with control devices that do not contain the sensitizing strip. To ensure that variations in the J-V characteristics are not strip-position dependent and are instead the result of minor sample-to-sample variations, the current density of each sensitized device at 5 V is plotted versus strip position in Figures 3d–f for D-EML, M-EML, and G-EML devices, respectively. The error bars are taken as the device-to-device variation observed for control devices fabricated in different runs. For each of the architectures, differences in the current densities do not trend systematically with sensitizer position, suggesting that the inclusion of the doped sensitizing strip does not substantially impact charge transport, satisfying condition (iii) discussed in Section 2.

The measured exciton recombination zone for a D-EML device is shown in **Figure 4**a at an applied current density of 10 mA cm^{-2} and is found to be pinned at the HTM:ETM interface. The total spatial extent of the recombination zone is ≈15 nm and does not shift in position or spatial extent throughout the range of current densities probed. Previous studies on the hole and electron mobilities of TCTA and BPhen have suggested that holes are slightly more mobile in TCTA than electrons in BPhen.[54,55] This is reflected here in the observation of an increased width in the recombination zone on the BPhen side of the D-EML. In terms of device operation, holes are arriving at the interface of the HTM:ETM more quickly and are penetrating into the ETM, likely by injection onto molecules of Ir(ppy)$_3$. The low concentration of Ir(ppy)$_3$ confines holes on the ETM side close to the interface, where they may form excitons with incoming electrons. More generally, the recombination zone in D-EML devices is dominated by the extent to which a minority carrier may penetrate the majority host. Minority charge carriers on each side of the D-EML are usually confined to the emissive guest in configurations where the guest energy levels lie within those of the host materials. To attain high η_{PL}, guest doping concentrations are typically <10 wt%, likely inhibiting efficient charge transport along the guest. Effectively, the product $n[x] \times p[x]$ is confined to a narrow region centered on the interface between the HTM and ETM in D-EML-based OLEDs.

The recombination zone profile of the M-EML device is shown in Figure 4b at an applied current density of 10 mA cm^{-2}. In comparison to the case of the D-EML, the recombination zone width in the M-EML is substantially larger, approaching a value of ≈40 nm. The peak exciton density is shifted towards the TCTA side of the M-EML, with the density decreasing to a negligible amount ≈40 nm from the TCTA/M-EML interface. The shape of the recombination zone is indicative of a device that is limited by the spatial extent of the hole density, potentially indicating that electrons are more mobile in the M-EML layer. Generally, the recombination zone in an M-EML-based device will depend on the transport properties of the emissive layer, transport layers, and blocking layers, but may be enhanced relative to

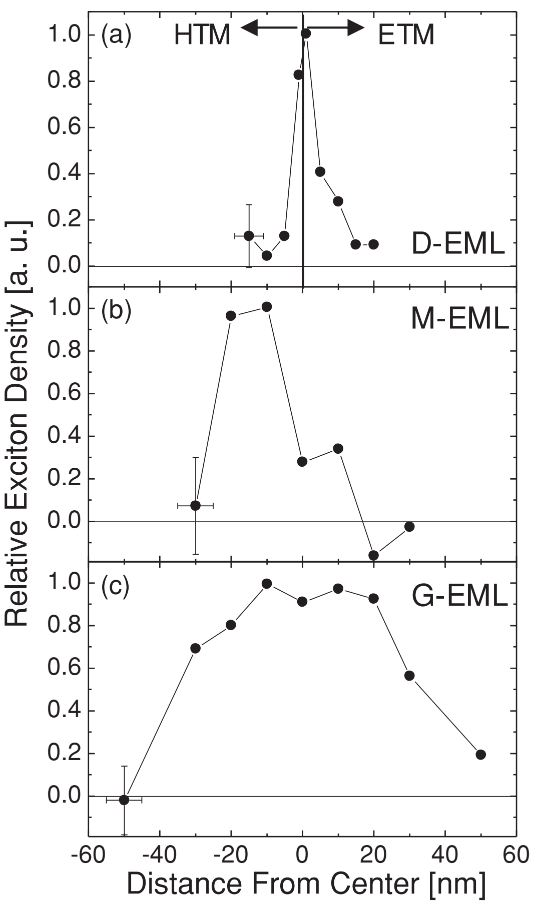

Figure 4. The relative exciton density versus position in a) D-EML, b) M-EML, and c) G-EML devices, at an applied current density of 10 mA cm^{-2}. For the D-EML device, the recombination zone is centered at the TCTA/BPhen interface and has a spatial extent of ≈15 nm. In the case of the M-EML device, the spatial extent of the recombination zone approaches ≈40 nm and is centered on the TCTA side of the emissive layer. The G-EML shows the largest recombination zone, with a spatial extent >80 nm, and is centered in the middle of the device.

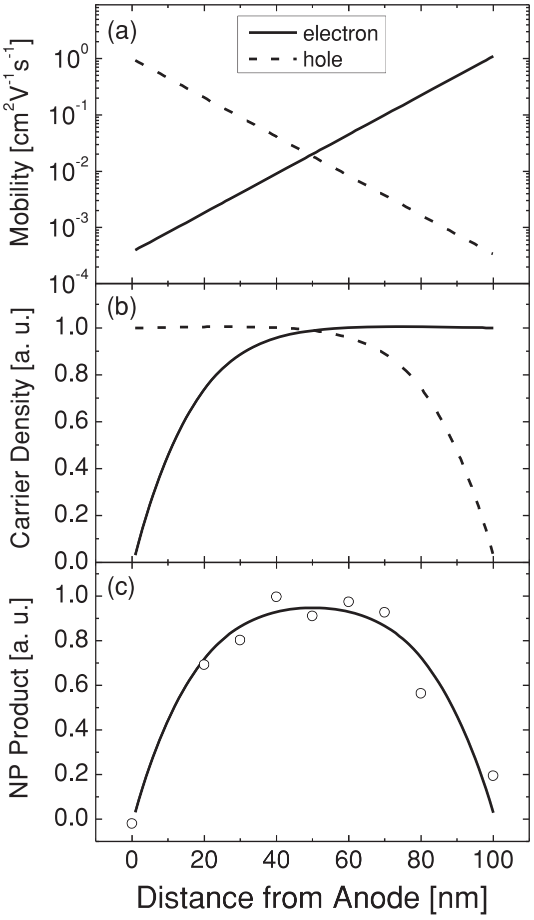

Figure 5. a) Functions chosen to describe the spatial variation of the electron and hole mobilities in a G-EML device. b) Calculated electron and hole densities; both carrier densities vanish at the opposing electrode, reflecting the boundary conditions and situation where there is no leakage current. c) The product *N*[X] × *P*[X] (NP product) is plotted along with the measured recombination zone data of Figure 4. The NP product has been scaled vertically, as the injected current density is arbitrarily set via the boundary condition in Equation 18.

the D-EML architecture due the ability of the M-EML to carry both electrons and holes.

The recombination zone profile of the G-EML is presented in Figure 4c for an applied current density of 10 mA cm^{-2} and spans the majority of the device, realizing a total spatial extent of >80 nm with a peak at the center of the layer. The measured exciton densities at the edge of the G-EML are within the experimental resolution of zero, indicating that excitons are not likely to form directly adjacent to the metal cathode. The large spatial extent of the recombination zone reflects a broad distribution of the electron and hole densities in the G-EML device. The observed symmetry and well-centered peak position in the exciton density is a result of the relative symmetry of the magnitude and spatial dependence of the electron and hole mobilities throughout the G-EML device.[30] Generally, it is expected that the spatial extent and peak location of the recombination zone in a G-EML-based OLED will reflect the spatial dependence of the electron and hole mobilities. This is addressed in the following section.

3.2. Electronic Model of G-EML

Using the boundary conditions described in Equations (17)-(20), the set of coupled differential equations describing the spatial overlap of the electron and hole densities have been solved numerically for the G-EML. The functions used to describe the spatial variation of the electron and hole mobilities of the TCTA:BPhen-based G-EML are shown in **Figure 5**a. These represent well the measured mobilities of a G-EML OLED described previously[30] using the same materials. In Figure 5b the spatial dependence of *N*[X] and *P*[X] is shown with the resulting NP product, *N*[X] × *P*[X], plotted in Figure 5c along with the experimentally measured recombination zone data, with the NP product scaled vertically. The simulated recombination zone matches well with measured data, reproducing both the peak position and breadth of the experimental data. In accordance with Equation (17) *N*[X] and *P*[X] vanish at the opposite electrode which drives the exciton density to zero,

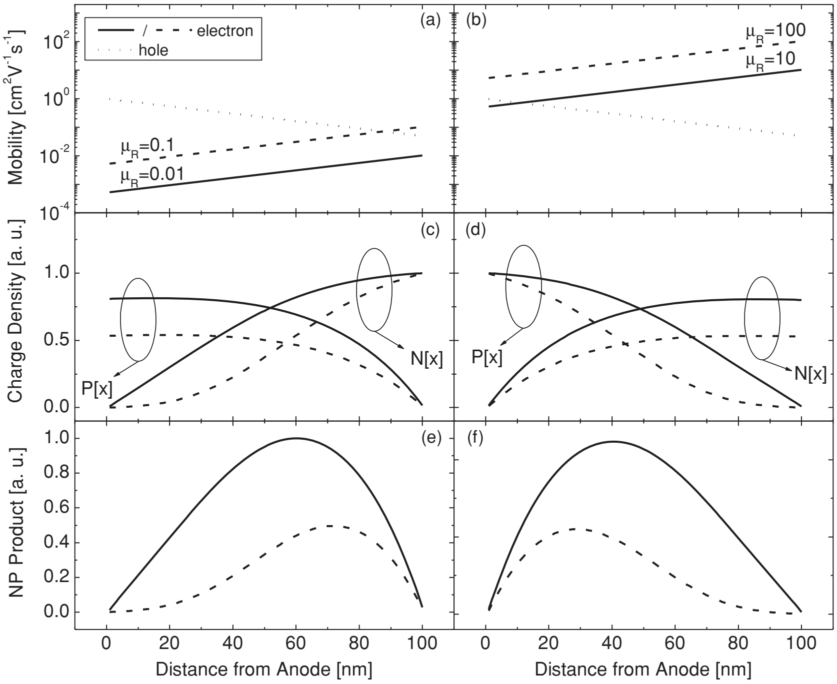

Figure 6. a) Spatial variation of electron and hole mobilities for G-EML devices where the ratio of electron to hole mobility is: $\mu_R = 0.01$and $\mu_R = 0.1$. b) Spatial variation of electron and hole mobilities for G-EML devices where $\mu_R = 10$ and $\mu_R = 100$. The calculated N[X] and P[X] for the mobilities shown in (a) and (b) are shown in (c) and (d), respectively. The resulting NP product of the carrier densities of (c) are shown in (e), while the NP product for the carrier densities of (d) are shown in (f).

confirming that no substantial exciton density is present near the electrodes in the G-EML device.

Given the good agreement between the model and experimental data, it is instructive to model the electron and hole charge densities, and NP product, for a series of G-EML devices which have HTM and ETM mobilities that are not well matched in magnitude, but retain the spatial dependence characteristic of the G-EML architecture. These simulations allow for characterization of the recombination zone in devices where particular materials may be desired due to beneficial optical properties, but where electrical transport may suffer. The magnitude and spatial dependence of the electron and hole mobilities examined are shown in **Figure 6**a,b. To simplify comparisons going forward, each case is identified by the ratio of the electron-to-hole mobility at the midpoint of the device, μ_R = 0.01, 0.1, 10, 100. The resulting N[X] and P[X] are shown in Figure 6c,d for μ_R = 0.01 and 0.1, and μ_R = 10 and 100, respectively. The NP products for μ_R = 0.01 and 0.1 is shown in Figure 6e, with the NP products for μ_R = 10 and 100 shown in Figure 6f.

For devices with a moderate mobility mismatch (i.e., μ_R between 0.01 and 100), the recombination zone is shifted away from the majority carrier injecting electrode, as seen in Figure 6c,d. The total extent of the recombination zone is not affected greatly, indicating the flexibility of the G-EML architecture to accommodate a wide range of HTM and ETM host combinations. For devices with large mobility mismatches, the recombination zone peak shifts greatly towards the minority carrier side. This is a result of the majority charge density extending far into the device. At extreme mobility mismatches the majority charge density extends far enough into the device that injected minority carriers rapidly encounter majority carriers, form excitons, and recombine. As the recombination zone encounters the electrode, additional losses may be incurred such as a loss in charge confinement, dissociation of the exciton by the nearby metal, or by exciton coupling to the surface plasmon modes.[56,57] These effects may be particularly important for devices with large mobility mismatches and have not been considered in this model as they apply to extreme cases where the HTM and ETM are poorly chosen.

Generally, in a G-EML-based device, materials with moderate mobility mismatches may be used by tuning the concentration gradient profile of the G-EML device. By tuning the relative deposition rates of the HTM, ETM, and guest material, a G-EML device with a composition favorable to electron or hole charge transport may be fabricated. Previously, a G-EML device with an electron-favorable composition profile was shown to be optimal for blue light-emitting devices.[30] These devices extend the minority carrier density further in to the device, improving electron-hole overlap while maintaining charge and exciton confinement, retaining the large recombination zone. High efficiency may then be realized in a wide range of simplified devices where particular active materials are desirable, despite a mismatch in mobilities.

3.3. Effects of Recombination Zone Width on Roll-Off

The four main parameters which govern the η_{EQE} roll-off of an OLED are: the relative rate constants of TTA and TPQ, τ, and the recombination zone width.[21,23] While the first three parameters depend primarily on materials selection, the recombination zone, as has been demonstrated here, is strongly device design-dependent. One way to quantitatively compare the efficiency roll-off of different architectures is to note the current density at which the η_{EQE} has rolled-off to half of its maximum, or "J_0."[21] Therefore, the peak-normalized η_{EQE} of the three device structures of interest are shown in **Figure 7**, with relevant device parameters presented in **Table 1**. Here, a reduction in the efficiency roll-off with current density is observed in devices characterized by a larger exciton recombination zone, as shown by an increased value for J_0 in the M-EML and G-EML structures relative to the D-EML. It is interesting to note that despite the larger recombination zone of the G-EML device relative to the M-EML, the efficiency roll-off in these devices is very similar. This may suggest that important parameters, such as the polaron density and the degree of charge confinement, differ significantly in each device. Further work is needed to fully quantify and decouple the role of the exciton recombination zone from other contributing factors that determine the efficiency roll-off.

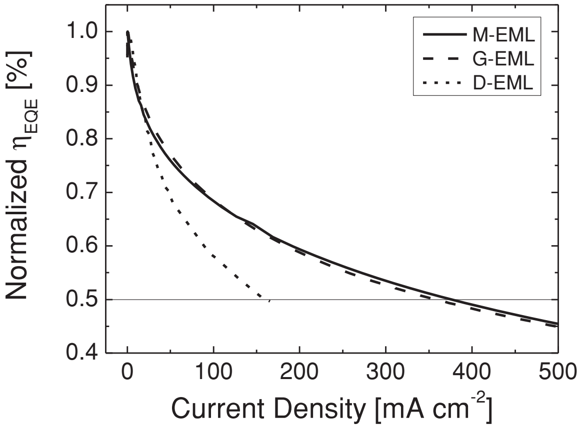

Figure 7. Peak-normalized η_{EQE} for D-EML, M-EML, and G-EML OLEDs. The J_0 for each device is: 160 mA cm^{-2}, 375 mA cm^{-2}, and 360 mA cm^{-2}, for D-EML, M-EML, and G-EML, respectively.

Table 1. Device parameters for the architectures of interest: Peak η_{EQE}, measured recombination zone (RZ) width, and roll-off parameter J_0, defined as the current density where η_{EQE} rolls-off to half its peak value, for the D-EML, M-EML, and G-EML device architectures.

Device Architecture	Peak η_{EQE} [%]	RZ [nm]	J_0 [mA cm^{-2}]
D-EML	11.8	15	160
M-EML	12.2	40	375
G-EML	16.9	80	360

4. Conclusions

A method to quantitatively measure the width and location of the exciton recombination zone in an OLED has been developed and is generally applicable and independent of emissive layer architecture. This technique demonstrates a high sensitivity to the presence of guest excitons, a high degree of spatial resolution, and does not alter charge transport in the OLED. We demonstrate a strong dependence of both the location and spatial extent of the exciton recombination zone on the emissive layer architecture. OLEDs based on M- and G-EML architectures have much larger recombination zones than devices based on a D-EML architecture, with the G-EML architecture showing a recombination zone which spans the entire device. This strong correlation emphasizes the need to couple efforts aimed at engineering OLED architecture with direct measurements of the exciton recombination zone. Quantitative insight into the exciton recombination zone is essential as a tool to guide OLED design and to better inform and evaluate critically needed models of operation.

5. Experimental Section

The Förster radius was calculated using the extinction coefficient of TPTBP as measured by spectroscopic ellipsometery, the photoluminescence spectrum of Ir(ppy)$_3$, an average index of refraction (n = 1.8) for the TCTA:BPhen host at the peak in Ir(ppy)$_3$ emission as determined by spectroscopic ellipsometery, and the photoluminescence quantum yield of Ir(ppy)$_3$, taken as $\eta_{PL} = 95\%$ based on previous work.[58] The formula weight of TPTBP is 816.99 g mol^{-1} and a density 1.2 g cm^{-1} was measured via X-ray reflectivity. Using Equation (2) and the above parameters, a Förster radius of R_0 = 3.9 nm is calculated. The Förster radius is primarily determined by the overlap of sensitizer absorption cross-section with the guest photoluminescence.

All devices are fabricated by vacuum thermal evaporation on glass substrates coated with a 150-nm-thick anode layer of indium-tin oxide (ITO) having a sheet resistance of 15 Ω/□. Substrates were cleaned and treated in UV-ozone ambient prior to film deposition. Green light-emitting devices were fabricated using 4,4',4''-tris(carbazol-9-yl)triphenylamine (TCTA, Sigma Aldrich) and 4,7-diphenyl-1,10-phenanthroline (BPhen, Alfa Aesar) as the HTM and ETM, respectively, with Ir(ppy)$_3$ (Kintec) as the luminescent guest and TPTBP (Frontier Scientific) as the quencher in sensitized devices; all materials were used as received. All organic layers were deposited in high vacuum (<10^{-7} Torr) with independent quartz crystal monitors measuring the deposition rate of each material, allowing for careful control of the concentration and location of TPTBP within the devices. The G-EML devices were fabricated using time-varying deposition rates as described previously,[11] with an optimal Ir(ppy)$_3$ doping concentration of 2 wt%. Sensitized G-EML devices included a 4-nm-thick strip of 1 wt% TPTBP with concentrations of TCTA, BPhen and Ir(ppy)$_3$ that are matched to the spatial location of the strip. The D-EML and M-EML devices were fabricated using the following optimized structures: ITO/40 nm TCTA:Ir(ppy)$_3$ (5 wt%)/40 nm BPhen:Ir(ppy)$_3$ (5 wt%) for the D-EML, and ITO/20 nm TCTA/60nm TCTA:BPhen:Ir(ppy)$_3$ (1:1:5 wt%)/20 nm BPhen for the M-EML. The additional TCTA and BPhen layers present in the M-EML device serve to confine charge the emissive layer; M-EML devices fabricated without such blocking layers have large leakage currents and show poor device performance.[11] Sensitized M-EML devices contained a 4-nm-thick strip of 1 wt% TPTBP and D-EML devices contained a 2-nm-thick strip of 1 wt% TPTBP with concentrations of TCTA, BPhen, and Ir(ppy)$_3$ corresponding to the spatial location within each device. The ratio of the strip width to measured recombination zone width remains <10% in all device architectures, ensuring a high degree of spatial accuracy. All devices were capped with a cathode consisting of a 1-nm-thick layer of LiF and 75-nm-thick layer of Al, evaporated through a shadow mask to define devices with a diameter of 1 mm. The current density-voltage and brightness-voltage characteristics of all devices were measured in ambient, following device fabrication. Measurements were performed using a calibrated Hamamatsu S3584-08 photodiode and an HP4155C parameter analyzer. The EL spectrum for each device was measured separately using a fiber-coupled Ocean Optics HR4000 spectrometer at current densities ranging from 0.1 to 10 mA cm^{-2}. Devices were centered on top of the optical fiber to ensure the maximum spectral output was recorded.

Acknowledgements

This work was supported primarily by the National Science Foundation (NSF) MRSEC Program under Award No. DMR-0819885. Support was also received from the University of Minnesota Initiative for Renewable Energy and the Environment. X-ray reflectivity measurements were carried out by Dr. M. Manno in the Characterization Facility, University of Minnesota, which receives partial support from NSF through the MRSEC program.

Received: January 9, 2013
Revised: March 7, 2013

---

[1] S. Watanabe, N. Ide, J. Kido, Jpn. *J. Appl. Phys.* **2007**, **46**, 1186.
[2] M. A. Baldo, D. F. O'Brien, Y. You, A. Shoustikov, S. Sibley, M. E. Thompson, S. R. Forrest, *Nature* **1998**, **395**, 151.

[3] M. E. Kondakova, T. D. Pawlik, R. H. Young, D. J. Giesen, D. Y. Kondakov, C. T. Brown, J. C. Deaton, J. R. Lenhard, K. P. Klubek, *J. Appl. Phys.* **2008**, *104*, 094501.

[4] J. Huang, M. Pfeiffer, A. Werner, J. Blochwitz, K. Leo, S. Liu, *Appl. Phys. Lett.* **2002**, *80*, 139.

[5] G. He, M. Pfeiffer, K. Leo, M. Hofmann, J. Birnstock, R. Pudzich, J. Salbeck, *Appl. Phys. Lett.* **2004**, *85*, 3911.

[6] J. Lee, C. Wu, S. Liu, C. Huang, Y. Chang, *Appl. Phys. Lett.* **2005**, *86*, 103506.

[7] C. Adachi, M. A. Baldo, M. E. Thompson, S. R. Forrest, *J. Appl. Phys.* **2001**, *90*, 5048.

[8] Z. W. Liu, M. G. Helander, Z. B. Wang, Z. H. Lu, *Appl. Phys. Lett.* **2009**, *94*, 113305.

[9] J. Meyer, S. Hamwi, T. Bulow, H. Johannes, T. Riedl, W. Kowalsky, *Appl. Phys. Lett.* **2007**, *91*, 113506.

[10] W. S. Jeon, T. J. Park, K. H. Kim, R. Pode, J. Jang, J. H. Kwon, *Org. Electron.* **2010**, *11*, 179.

[11] N. C. Erickson, R. J. Holmes, *Appl. Phys. Lett.* **2010**, *97*, 083308.

[12] M. Furno, R. Meerheim, S. Hofmann, B. Lüssem, K. Leo, *Phys. Rev. B* **2012**, *85*, 115205.

[13] M. Schober, M. Anderson, M. Thomschke, J. Widmer, M. Furno, R. Scholz, B. Lüssem, K. Leo, *Phys. Rev. B* **2011**, *84*, 165326.

[14] I. Park, S. Park, D. Shin, J. Oh, W. Song, J. Yoon, *Org. Electron.* **2010**, *11*, 218.

[15] V. Bulovi , V. B. Khalfin, G. Gu, P. E. Burrows, D. Z. Garbuzov, S. R. Forrest, *Phys. Rev. B* **1998**, *58*, 3730.

[16] T. Cho, C. Lin, C. Wu, *Appl. Phys. Lett.* **2006**, *88*, 111106.

[17] E. F. Schubert, N. E. J. Hunt, M. Micovic, R. J. Malik, D. L. Sivco, A. Y. Cho, G. J. Zydzik, *Science* **1994**, *265*, 943.

[18] Q. Huang, S. Reineke, K. Walzer, M. Pfeiffer, K. Leo, *Appl. Phys. Lett.* **2006**, *89*, 263512.

[19] S. Mladenovski, S. Reineke, K. Neyts, *Opt. Lett.* **2009**, *34*, 1375.

[20] D. Song, S. Zhao, H. Aziz, *Adv. Funct. Mater.* **2011**, *21*, 2311.

[21] M. A. Baldo, C. Adachi, S. R. Forrest, *Phys. Rev. B* **2000**, *62*, 10967.

[22] N. C. Giebink, S. R. Forrest, *Phys. Rev. B* **2008**, *77*, 235215.

[23] S. Reineke, K. Walzer, K. Leo, *Phys. Rev. B* **2007**, *75*, 125328.

[24] J. Kalinowski, W. Stampor, J. M yk, M. Cocchi, D. Virgili, V. Fattori, P. Di Marco, *Phys. Rev. B* **2002**, *66*, 235321.

[25] J. Kalinowski, W. Stampor, J. Szmytkowski, D. Virgili, M. Cocchi, V. Fattori, C. Sabatini, *Phys. Rev. B* **2006**, *74*, 085316.

[26] S. Reineke, G. Schwartz, K. Walzer, K. Leo, *Phys. Status Solidi RRL* **2009**, *3*, 67.

[27] D. Song, S. Zhao, Y. Luo, H. Aziz, *Appl. Phys. Lett.* **2010**, *97*, 243304.

[28] W. Staroske, M. Pfeiffer, K. Leo, M. Hoffmann, *Phys. Rev. Lett.* **2007**, *98*, 197402.

[29] L. Bozano, S. A. Carter, J. C. Scott, G. G. Malliaras, P. J. Brock, *Appl. Phys. Lett.* **1999**, *74*, 1132.

[30] N. C. Erickson, R. J. Holmes, *J. Appl. Phys.* **2011**, *110*, 084515.

[31] C. Hsiao, Y. Chen, T. Lin, C. Hsiao, J. Lee, *Appl. Phys. Lett.* **2006**, *89*, 163511.

[32] S. Su, E. Gonmori, H. Sasabe, J. Kido, *Adv. Mater.* **2008**, *20*, 4189.

[33] X. Zhou, D. S. Qin, M. Pfeiffer, J. Blochwitz-Nimoth, A. Werner, J. Drechsel, B. Maennig, K. Leo, M. Bold, P. Erk, H. Hartmann, *Appl. Phys. Lett.* **2002**, *81*, 4070.

[34] J. Lee, J. Lee, J. Y. Lee, H. Y. Chu, *Appl. Phys. Lett.* **2009**, *94*, 193305.

[35] S. Liu, J. Lee, C. Lee, C. Chen, J. Wang, *Appl. Phys. Lett.* **2007**, *91*, 142106.

[36] S. H. Kim, J. Jang, J. Y. Lee, *Appl. Phys. Lett.* **2007**, *91*, 083511.

[37] U. S. Bhansali, H. Jia, M. A. Q. Lopez, B. E. Gnade, W. Chen, M. A. Omary, *Appl. Phys. Lett.* **2009**, *94*, 203501.

[38] M. C. Gather, M. Flammich, N. Danz, D. Michaelis, K. Meerholz, *Appl. Phys. Lett.* **2009**, *94*, 263301.

[39] J. Kalinowski, L. C. Palilis, W. H. Kim, Z. H. Kafafi, *J. Appl. Phys.* **2003**, *94*, 7764.

[40] J. Lee, J. Lee, K. Song, S. J. Lee, H. Y. Chu, *Appl. Phys. Lett.* **2008**, *92*, 133304.

[41] S. L. M. van Mensfoort, M. Carvelli, M. Megens, D. Wehenkel, M. Bartyzel, H. Greiner, R. A. J. Janssen, R. Coehoorn, *Nat. Photonics* **2010**, *4*, 329.

[42] N. Chopra, J. Lee, Y. Zheng, S. Eom, J. Xue, F. So, *ACS Appl. Mater. Interfaces* **2009**, *1*, 1169.

[43] W. H. Choi, C. H. Cheung, S. K. So, *Org. Electron.* **2010**, *11*, 872.

[44] R. J. Holmes, B. W. D'Andrade, S. R. Forrest, X. Ren, J. Li, M. E. Thompson, *Appl. Phys. Lett.* **2003** *83*, 3818.

[45] C. Weichsel, L. Burtone, S. Reineke, S. I. Hintschich, M. C. Gather, K. Leo, B. Lüssem, *Phys. Rev. B* **2012**, *86*, 075204.

[46] S. Lee, C. W. Tang, *J. Vac. Sci. Technol., B* **2011**, *29*, 062401.

[47] M. Pope, C. E. Swenberg, *Electronic Processes in Organic Crystals*, Oxford University Press, New York **1982**.

[48] N. J. Turro, *Modern Molecular Photochemistry*, University Science Books, CA **1991**.

[49] T. Förster, *Discuss. Faraday Soc.***1959***27*, 7.

[50] J. Staudigel, M. Stossel, F. Steuber, J. Simmerer, *J. Appl. Phys.* **1999**, *86*, 3895.

[51] F. Neumann, Y. A. Genenko, R. Schmechel, H. von Seggern, *Synth. Met.* **2005**, *150*, 291.

[52] R. Coehoorn, S. L. M. van Mensfoort, *Phys. Rev. B* **2009**, *80*, 085302.

[53] G. G. Malliaras, J. C. Scott, *J. Appl. Phys.* **1999**, *85*, 7426.

[54] S. Noh, C. K. Suman, Y. Hong, C. Lee, *J. Appl. Phys.* **2009**, *105*, 033709.

[55] S. Naka, H. Okada, H. Onnagawa, T. Tsutsui, *Appl. Phys. Lett.* **2000**, *76*, 197.

[56] P. A. Hobson, S. Wedge, J. A. E. Wasey, I. Sage, W. L. Barnes, *Adv. Mater.* **2002**, *14*, 1393.

[57] L. H. Smith, J. A. E. Wasey, W. L. Barnes, *Appl. Phys. Lett.* **2004**, *84*, 2986.

[58] Y. Kawamura, K. Goushi, J. Brooks, J. J. Brown, H. Sasabe, C. Adachi, *Appl. Phys. Lett.* **2005**, *86*, 071104.